

Generalizing diffuse interface methods on graphs: non-smooth potentials and hypergraphs

Jessica Bosch, Steffen Klamt, and Martin Stoll

Abstract—Diffuse interface methods have recently been introduced for the task of semi-supervised learning. The underlying model is well-known in materials science but was extended to graphs using a Ginzburg–Landau functional and the graph Laplacian. We here generalize the previously proposed model by a non-smooth potential function. Additionally, we show that the diffuse interface method can be used for the segmentation of data coming from hypergraphs. For this we show that the graph Laplacian in almost all cases is derived from hypergraph information. Additionally, we show that the formerly introduced hypergraph Laplacian coming from a relaxed optimization problem is well suited to be used within the diffuse interface method. We present computational experiments for graph and hypergraph Laplacians.

Index Terms—Diffuse interface methods, Newton method, Iterative algorithms, Semisupervised learning, Equations

I. INTRODUCTION

The classification of high-dimensional data on graphs is a challenging problem in many application areas [1], [2] and several techniques have been developed to efficiently tackle this problem. Recently, Bertozzi and Flenner [3] have established a method on the interface of graph based methods and partial differential equations (PDEs). Their method, which has already been extended to other cases (see [4], [5]), utilizes the information of the underlying graph via its graph Laplacian and then uses diffuse interface techniques for the separation of the given data into two classes. Diffuse interface techniques are a classical tool within the materials science community [6], [7]. The new technique of Bertozzi and Flenner uses an approach taken from image inpainting based on phase-field methods [8] for a semi-supervised learning problem. The use of phase-field models in image processing has seen many contributions (cf. [9], [10]).

To further use the inpainting analogy in the semi-supervised learning problem, the known or sampled data, which are used to train the method, can be considered the intact part of the image and we aim to restore the damaged or unknown part of the image. This works for both segmentation into two classes for binary images or into multiple classes for gray-valued or color images. PDE-based inpainting has been very successful [11] and the technique introduced in [3] showed very promising results when compared to other methods such as the 1-Laplacian inverse power method (IPM) of Hein and Bühler [12].

M. Stoll and S. Klamt are with the Max Planck Institute for Dynamics of Complex Technical Systems, Sandtorstr. 1, 39106 Magdeburg, Germany (stollm@mpi-magdeburg.mpg.de, klamt@mpi-magdeburg.mpg.de). J. Bosch is with the Department of Computer Science, The University of British Columbia, 201-2366 Main Mall, Vancouver, BC V6T 1Z4, Canada (jbosch@cs.ubc.ca).

Our goal in this paper is the extension of the diffuse interface technique from using smooth potentials to the case of non-smooth potentials as well as the introduction of the diffuse interface approach when applied to hypergraph based segmentation. Non-smooth potentials are now widely used in many materials science applications [13], [14] and our previous work [15], [16] in image processing illustrated their importance also for image inpainting. The incorporation of these potentials into the graph based approach requires the use of an additional non-linear solver for which we propose a semi-smooth Newton method [17]. Furthermore, we show that the segmentation is not limited to two classes but extend this to the multiclass segmentation problem as considered in [4]. Additionally, we aim at showing that the approach from [3] is so general that the underlying structural information do not necessarily have to come from the graph Laplacian but that the often very natural hypergraph formulation is well-suited for the combination with phase-field approaches both with smooth and non-smooth potentials.

We start our discussion by introducing the graph Laplacian and the computation of some of its smallest eigenvalues. We then introduce the diffuse interface technique introduced in [3] and extend it to the case when a non-smooth potential is used. This is done both for the two-classes segmentation problem as well as the multiclass segmentation. We further extend the existing approaches by illustrating the applicability of diffuse interface methods on hypergraphs. Numerical results illustrate that the proposed methods work well on many test problems.

II. THE GRAPH LAPLACIAN AND FUNDAMENTALS

We here consider an undirected graph $G = (V, E)$ consisting of a vertex set $V = \{x_i\}_{i=1}^n$ and the edge set E [18]. Each edge $e \in E$ is a pair of nodes (x_i, x_j) with $x_i \neq x_j$ and $x_i, x_j \in V$. For a weighted graph we also have a weight function $w : V \times V \rightarrow \mathbb{R}$ with $w(x_i, x_j) = w(x_j, x_i)$ for all i, j for an undirected graph. We assume further that the function is positive for existing edges and zero otherwise. The degree of the vertex $x_i \in V$ is defined as

$$d(x_i) = \sum_{x_j \in V} w(x_i, x_j).$$

The diagonal degree matrix $D \in \mathbb{R}^{n,n}$ is defined as $D_{i,i} = d(x_i)$. Now the crucial tool for further investigations is the graph Laplacian L which is defined via

$$L(x_i, x_j) = \begin{cases} d(x_i) & \text{if } x_i = x_j \\ -w(x_i, x_j) & \text{otherwise.} \end{cases}$$

It is clear that we can write $L = D - W$ with the entries of the weight matrix W_{ij} given by $w(x_i, x_j)$. The Laplacian

in this form is rarely used as typically its normalized form [19] is employed for segmentation purposes. The normalized Laplacian is defined by

$$L_s = D^{-1/2}LD^{-1/2} = I - D^{-1/2}WD^{-1/2},$$

which is a symmetric matrix. In contrast another normalized Laplacian of nonsymmetric form is given by

$$L_w = D^{-1}L = I - D^{-1}W.$$

We will use the eigenvalues of the symmetric and normalized graph Laplacian for numerical purposes later. We now discuss possibilities to compute the eigenvalues and eigenvectors of the matrix L_s .

A. Computing eigenvalues of the Laplacian

In practice the computation of several small eigenvalues of a matrix is a very challenging task. For small to moderate sizes the QR algorithm [20] is the method of choice for the computation of all eigenvalues of a matrix. For the computation of a subset of the eigenvalues the Lanczos algorithm for symmetric matrices and the Arnoldi algorithm for nonsymmetric matrices are typically chosen if the matrix is large and sparse [21]. For large and sparse graphs the Laplacian will also be large and sparse and the authors in [3], [4] suggest a Rayleigh-Chebyshev procedure [22]. Since the matrix is semi-definite a straightforward inverse iteration cannot be employed. One could consider projection techniques [23] and employing suitable preconditioners is possible [24]. Our goal (cf. [25]) is to compute the k smallest eigenvalues of $L_s = D^{-1/2}LD^{-1/2} = I - D^{-1/2}WD^{-1/2}$. For this it is clear that one could also focus on the largest eigenvalues λ_j of the matrix $D^{-1/2}WD^{-1/2}$ as the eigenvalues of L_s are given via $1 - \lambda_j$. One could use the Lanczos method for the computation of the largest eigenvalues as this method only requires the multiplication by the matrices $D^{-1/2}$ and W . Here the dominating cost is given by the application of W , which potentially could be a dense matrix depending on the structure of the graph. To avoid such an expensive step a more advanced method was proposed by Bertozzi and Flenner in [3]. They introduce the well-known Nyström extension [26], [27], which can work with submatrices of L_s that are of much smaller dimension. The method operates by approximating the eigenpairs of $D^{-1/2}WD^{-1/2}$ using a quadrature rule with randomly chosen interpolation points. For simplicity, we will rely on the Lanczos process for $D^{-1/2}WD^{-1/2}$ via MATLAB's `eigs` function but recommend the use of randomized methods, such as the Nyström extension, for large-scale graph segmentation.

B. Weight function

The choice of weight functions $w(x_i, x_j)$ is a crucial ingredient in the construction of the graph Laplacian. This choice will influence the performance of the segmentation process and the speed of the algorithm. This means that different choices of w result in different segmentation results. The graph Laplacian will be crucially influenced by the weight matrix W . For example a sparse matrix W will allow a much easier

computation of the eigenvalues of L_s . This means for complete graphs that the weight matrix needs to neglect certain relations between nodes whereas sparse graphs automatically result in sparse weight matrices.

Typical choices for $w(x_i, x_j)$ are the Gaussian function

$$w(x_i, x_j) = \exp\left(-\frac{\text{dist}(x_i, x_j)^2}{\sigma}\right) \quad (1)$$

for some scaling parameter σ and different choices for the metric $\text{dist}(x_i, x_j)$ result in different methods. Another popular choice was introduced by Zelnik-Manor and Perona [28] as

$$w(x_i, x_j) = \exp\left(-\frac{\text{dist}(x_i, x_j)^2}{\sqrt{\tau(x_i)\tau(x_j)}}\right) \quad (2)$$

where $\tau(x_i) = \text{dist}(x_i, x_k)$ and $\tau(x_j) = \text{dist}(x_j, x_k)$ are local scalings of the weight to the R -th nearest neighbour¹. It is clear that for the application in image processing the distance $\text{dist}(x, y)$ is the difference between intensities of the pixels y and x . For color images this will be the sum of distances within the different channels. For other applications, e.g. machine learning, $\text{dist}(x_i, x_j)$ could measure the Euclidean distance between the corresponding feature vectors (cf. [3]) of x_i and x_j . We have now the ingredients to compute the graph Laplacian as well as approximating k of its smallest eigenvalues and introduce the diffuse interface techniques next.

III. DIFFUSE INTERFACE METHODS ON GRAPHS WITH NON-SMOOTH POTENTIALS

A. Diffuse interface methods

Diffuse interface methods are a classical and versatile tool in the simulation of materials science problems such as solidification processes [7], [29]. They are an indispensable tool for the simulation of phase separation processes but have over time spread to various other application areas ranging from biomembrane simulation [30] to image inpainting [8], [15].

As these methods describe the separation of a mixed medium into two or more phases this methodology was recently extended by Bertozzi and Flenner [3]. These techniques, which are typically formulated in an infinite-dimensional setting, are now used within a graph-based formulation. The derivation of classical models such as the Allen-Cahn [7] or Cahn-Hilliard equations [29] is typically obtained from a gradient flow of the Ginzburg-Landau energy

$$E(u) = \int \frac{\varepsilon}{2} |\nabla u|^2 dx + \int \frac{1}{\varepsilon} \psi(u) dx \quad (3)$$

where u is the phase-field and ε the interface parameter, which is typically assumed to be small. The function $\psi(u)$ is a potential that forces the phase-field u to take values at either $u \approx -1$ or $u \approx 1$. We come back to the discussion of the choice of potential as this is one of the contributions of this paper. The minimization of the energy $E(u)$ follows a gradient flow, i.e.,

$$\partial_t u = -\text{grad}(E(u)).$$

¹For the MATLAB© codes computing the graph Laplacian we refer to <http://www.vision.caltech.edu/lihi/Demos/SelfTuningClustering.html>.

Different choices for the gradient lead to different evolution equations for the phase u . We here point to the well-known Allen–Cahn equation written as

$$\partial_t u = \varepsilon \Delta u - \varepsilon^{-1} \psi'(u) \quad (4)$$

with given initial condition u_0 and zero Neumann boundary conditions. Here, $\psi'(u)$ is the derivative of a smooth potential $\psi(u)$. In the case of a non-smooth potential we obtain a variational inequality. The Allen–Cahn equation has also been used very successfully in image inpainting [31], [32]. For this purpose Equation (4) is modified

$$\partial_t u = \varepsilon \Delta u - \varepsilon^{-1} \psi'(u) + \omega(x)(f - u) \quad (5)$$

where $\omega(x)$ is a parameter that is zero in the damaged image domain D and typically a large constant ω_0 in the intact parts $\Omega \setminus D$. Here f is the given image that we do not want to change in the undamaged part.

B. Diffuse interface methods on graphs

In a very similar way, Bertozzi and Flenner formulated the semi-supervised learning problem. Here f represents the learned data that have to be maintained throughout the evolution process. We want to derive a model that separates the domain Ω into two parts, i.e., two phases. The formulation for arbitrary information is inherently different as the Ω describes a set of points that we want to segment into two categories. For this the infinite-dimensional problem (4) is now defined using the description of the underlying graph Laplacian L_s to given

$$E_s(u) = \frac{\varepsilon}{2} u \cdot L_s u + \sum_{x \in V} \frac{1}{\varepsilon} \psi(u(x)) + F(f, u) \quad (6)$$

with the energy contribution $F(f, u)$ describing the fidelity term that would lead to $\omega(x)(f - u)$ in the continuous Allen–Cahn equation. Here, $u \cdot L_s u$ is defined via

$$\frac{\varepsilon}{2} u \cdot L_s u = \frac{\varepsilon}{2} \sum_{x_i, x_j} \frac{w(x_i, x_j)(u(x_i) - u(x_j))^2}{d(x_i, x_j)}$$

and if $u = 1$ in the set A and $u = -1$ in \bar{A} one obtains

$$\begin{aligned} \frac{\varepsilon}{2} u \cdot L_s u &= \frac{\varepsilon}{2} \sum_{\substack{x_i \in A, x_j \in \bar{A} \\ \text{or } x_i \in \bar{A}, x_j \in A}} \frac{w(x_i, x_j)(u(x_i) - u(x_j))^2}{d(x_i, x_j)} \\ &= \frac{4\varepsilon}{2} \sum_{\substack{x_i \in A, x_j \in \bar{A} \\ \text{or } x_i \in \bar{A}, x_j \in A}} \frac{w(x_i, x_j)}{d(x_i, x_j)}. \end{aligned}$$

This clearly indicates that $u \cdot L_s u$ is minimal if the weights across the interface, i.e. in between values from A and \bar{A} , are minimized. For a more detailed discussion of the comparison of diffuse interface methods to other segmentation methods such as graph cuts and nonlocal means we refer to [3].

We are now ready to write down the corresponding Allen–Cahn equation for the graph Laplacian as

$$u_t = -\varepsilon L_s u - \varepsilon^{-1} \psi'(u) + \omega(x)(f - u) \quad (7)$$

(see [33], [34] for details). Before discussing the details of the discretization we introduce a convexity splitting scheme that has been used very effectively for Cahn–Hilliard and Allen–Cahn equations with fidelity terms (see [8], [35], [36], [15]). For this the energy is split as

$$E(u) = E_1(u) - E_2(u)$$

with

$$E_1(u) = \int \frac{\varepsilon}{2} |\nabla u|^2 dx + \int \frac{c}{2} |u|^2 dx$$

and

$$E_2(u) = - \int \frac{1}{\varepsilon} \psi(u) dx + \int \frac{c}{2} |u|^2 dx - \int \frac{\omega(x)}{2} (f - u)^2 dx.$$

Using an implicit Euler for E_1 and explicit treatment for E_2 for the temporal evolution results in

$$\begin{aligned} \frac{u(x) - \bar{u}(x)}{\tau} - \varepsilon \Delta u(x) + cu(x) \\ = -\frac{1}{\varepsilon} \psi'(\bar{u}(x)) + c\bar{u}(x) + \omega(x)(f - \bar{u}(x)). \end{aligned}$$

Note we did not introduce an index for the temporal discretization but rather assume that all values $u(x)$ are evaluated at the new time-point whereas \bar{u} indicates the previous time-point. These equations are a model based on the infinite-dimensional formulation but our goal is to use the graph Laplacian based formulation as introduced in [3]. We obtain the same equations when our formulation is based on the graph Ginzburg–Landau energy, i.e.,

$$\begin{aligned} \frac{u(x) - \bar{u}(x)}{\tau} + \varepsilon L_s u(x) + cu(x) \\ = -\frac{1}{\varepsilon} \psi'(\bar{u}(x)) + c\bar{u}(x) + \omega(x)(f - \bar{u}(x)), \end{aligned}$$

where the dimensionality of u is adjusted to the size of the graph Laplacian. Assuming that (λ_j, ϕ_j) are the eigenpairs of L_s we can write $u(x) = \sum_{k=1}^m \mathbf{u}_k \phi_k$ and from this we get

$$\frac{\mathbf{u}_k - \bar{\mathbf{u}}_k}{\tau} + \varepsilon \lambda_k \mathbf{u}_k + c\mathbf{u}_k = -\frac{1}{\varepsilon} \bar{\mathbf{b}}_k + c\bar{\mathbf{u}}_k + \bar{\mathbf{d}}_k \quad (8)$$

where $\bar{\mathbf{b}} = \psi'(\sum_{k=1}^m \bar{\mathbf{u}}_k \phi_k)$ and $\bar{\mathbf{d}} = \omega(f - \sum_{k=1}^m \bar{\mathbf{u}}_k \phi_k)$. We further rewrite this to obtain

$$(1 + \varepsilon \tau \lambda_k + c\tau) \mathbf{u}_k = \frac{\tau}{\varepsilon} \bar{\mathbf{b}}_k + (1 + c\tau) \bar{\mathbf{u}}_k + \tau \bar{\mathbf{d}}_k. \quad (9)$$

With the choice of $\psi(u) = \frac{1}{4}(u^2 - 1)^2$ we obtain the scheme introduced in [3].

C. Non-smooth potentials

In classical phase-field simulations the choice of potential function typically plays a crucial role and non-smooth potentials have proven to allow for the most realistic reproductions of processes in materials science. For this the well-known obstacle potential can be used. In more detail, we consider

$$\psi_{ns}(u) := \begin{cases} \frac{1}{2}(1 - u^2), & -1 \leq u \leq 1 \\ \infty, & \text{otherwise,} \end{cases} \quad (10)$$

and obtain the following modified Allen–Cahn equation

$$\partial_t u = \varepsilon \Delta u - \frac{1}{\varepsilon} (\psi'_0(u) + \mu) + \omega(x)(f - u), \quad (11)$$

$$\mu \in \partial\beta_{[-1,1]}(u), \quad (12)$$

$$-1 \leq u \leq 1, \quad (13)$$

$$\frac{\partial u}{\partial n} = \frac{\partial \Delta u}{\partial n} = 0 \quad \text{on } \partial\Omega. \quad (14)$$

Here we have written ψ_{ns} in (10) via the indicator function as

$$\psi_{ns}(u) = \psi_0(u) + I_{[-1,1]}(u)$$

and $\psi_0(u) := \frac{1}{2}(1 - u^2)$. We now follow a well-known approach by regularizing the energy with the Moreau-Yosida penalty term [16], [37] and obtain

$$E(u_\nu) = \int_\Omega \frac{\varepsilon}{2} |\nabla u_\nu|^2 + \frac{1}{\varepsilon} \psi_0(u_\nu) + \frac{1}{2\nu} |\max(0, u_\nu - 1)|^2 + \frac{1}{2\nu} |\min(0, u_\nu + 1)|^2 dx,$$

with ν the penalty parameter. Again, we consider the convexity splitting for this energy and obtain

$$E_1(u_\nu) = \int \frac{\varepsilon}{2} |\nabla u_\nu|^2 dx + \int \frac{c}{2} |u_\nu|^2 dx + \int \frac{1}{2\nu} |\max(0, u_\nu - 1)|^2 + \frac{1}{2\nu} |\min(0, u_\nu)|^2 dx$$

and

$$E_2(u_\nu) = - \int \frac{1}{\varepsilon} \psi_0(u_\nu) dx + \int \frac{c}{2} |u_\nu|^2 dx - \int \frac{\omega(x)}{2} (f - u_\nu)^2 dx.$$

This leads to the following evolution equation

$$\frac{u_\nu - \bar{u}_\nu}{\tau} - \varepsilon \Delta u_\nu + c u_\nu + \theta_\nu(u_\nu) = -\frac{1}{\varepsilon} \psi'_0(\bar{u}) + c \bar{u} + \omega(f - \bar{u}), \quad (15)$$

where

$$\theta_\nu(u_\nu) := \frac{1}{\nu} \max(0, u_\nu - 1) + \frac{1}{\nu} \min(0, u_\nu + 1).$$

In the previous setup the nonlinearity coming from the potential term was shifted towards the right-hand side as it was treated explicitly. In the non-smooth setting we obtain a nonlinear relation due to the non-smooth relation given by $\theta_\nu(u_\nu)$, which we treat with the well-known semi-smooth Newton method [17]. For (15) written as

$$F(u_\nu) = (c + \frac{1}{\tau})u_\nu - \varepsilon \Delta u_\nu + \theta_\nu(u_\nu) + \frac{1}{\varepsilon} \psi'_0(\bar{u}) - (c + \frac{1}{\tau})\bar{u} - \omega(f - \bar{u}) = 0$$

the Newton system is given via

$$u_\nu^{(l+1)} = u_\nu^{(l)} - G(u_\nu^{(l)})^{-1} F(u_\nu^{(l)}).$$

We define the sets

$$\mathcal{A}(u_\nu) := \{x \in \Omega : u_\nu > 1 \text{ or } u_\nu < -1\},$$

$$\mathcal{A}_+(u_\nu) := \{x \in \Omega : u_\nu > 1\},$$

$$\mathcal{A}_-(u_\nu) := \{x \in \Omega : u_\nu < -1\},$$

and write down the Newton system as

$$\begin{aligned} G(u_\nu^{(l)})u_\nu^{(l+1)} &= G(u_\nu^{(l)})u_\nu^{(l)} - F(u_\nu^{(l)}) \\ &= -\nu^{-1} \left(\chi_{\mathcal{A}_-(u_\nu^{(l)})} - \chi_{\mathcal{A}_+(u_\nu^{(l)})} \right) \mathbf{1} + \left(\frac{1}{\varepsilon} + c + \frac{1}{\tau} \right) \bar{u} \\ &\quad + \omega(f - \bar{u}) \end{aligned}$$

where $G(u_\nu^{(l)}) := (c + \frac{1}{\tau})I - \varepsilon \Delta + \frac{1}{\nu} \chi_{\mathcal{A}(u_\nu^{(l)})}$ with I the identity operator. Again, we have first introduced the classical problem. The equivalent formulation using the graph Laplacian is given via

$$\begin{aligned} \frac{u_\nu - \bar{u}_\nu}{\tau} + \varepsilon L_s u_\nu + c u_\nu + \theta_\nu(u_\nu) &= -\frac{1}{\varepsilon} \psi'_0(\bar{u}) + c \bar{u} + \omega(f - \bar{u}), \quad (16) \end{aligned}$$

and we obtain the Newton system

$$\begin{aligned} G(u_\nu^{(l)})u_\nu^{(l+1)} &= -\nu^{-1} \left(\chi_{\mathcal{A}_-(u_\nu^{(l)})} - \chi_{\mathcal{A}_+(u_\nu^{(l)})} \right) \mathbf{1} \\ &\quad + \left(\frac{1}{\varepsilon} + c + \frac{1}{\tau} \right) \bar{u} + \omega(f - \bar{u}) \end{aligned}$$

where $G(u_\nu^{(l)}) := (c + \frac{1}{\tau})I + \varepsilon L_s + \frac{1}{\nu} \chi_{\mathcal{A}(u_\nu^{(l)})}$ with I the identity matrix. In the following we drop the index ν . This Newton system is the equivalent to the infinite dimensional Newton system and in a Galerkin fashion we assume $u^{(l)} = \sum_{k=1}^m \mathbf{u}_{k,l} \phi_k = \Phi \mathbf{u}^{(l)}$ with a small number m of terms chosen as the projection basis. This results in the projected system

$$\begin{aligned} \Phi^T G(u^{(l)}) \Phi \mathbf{u}^{(l+1)} &= -\frac{1}{\nu} \Phi^T \left(\chi_{\mathcal{A}_-(u^{(l)})} - \chi_{\mathcal{A}_+(u^{(l)})} \right) \mathbf{1} \\ &\quad + \left(\frac{1}{\varepsilon} + c + \frac{1}{\tau} \right) \Phi^T \Phi \bar{\mathbf{u}} + \Phi^T \omega(f - \Phi \bar{\mathbf{u}}). \quad (17) \end{aligned}$$

Here the crucial operator becomes

$$\Phi^T G(u^{(l)}) \Phi = (c + \frac{1}{\tau})I + \varepsilon \Lambda + \frac{1}{\nu} \Phi^T \chi_{\mathcal{A}(u^{(l)})} \Phi$$

where Λ is the diagonal matrix containing the m eigenvalues used in the approximation. It is clear that (17) requires the solution of a small $m \times m$ linear system for which we use the CG method [38] or use a direct solver based on a factorisation of the matrix.

IV. DIFFUSE INTERFACE METHODS ON GRAPHS – THE VECTOR-VALUED CASE

A. Vector-valued smooth diffuse interface methods

Section III was devoted to scalar diffuse interface models on graphs. In this section, we present their generalization to the vector-valued case. This can then be used for the multiclass segmentation problem.

In practice, often more than two components occur; see, e.g., the biomembrane simulation [30], image inpainting of gray value images [16], as for this the diffuse interface models have been extended to deal with multi-component systems. The Ginzburg–Landau energy for two components in (3) generalizes to

$$E(\mathbf{u}) = \int \frac{\varepsilon}{2} \sum_{i=1}^K |\nabla u_i|^2 dx + \int \frac{1}{\varepsilon} \psi(\mathbf{u}) dx \quad (18)$$

for $K > 2$ components. Here, $\mathbf{u} = (u_1, \dots, u_K)^T$ is now the vector-valued phase-field, and the potential function $\psi(\mathbf{u})$ has K distinct minima instead of two. This section deals with smooth potentials, and the smooth potential in the scalar case generalizes to the vector-valued case as $\psi(\mathbf{u}) = \frac{1}{4} \sum_{i=1}^K u_i^2 (1 - u_i)^2$. We come back to the discussion of non-smooth potentials in Section IV-B.

Recently, Garcia-Cardona et al. [4] as well as Merkurjev et al. [5] have extended these continuous models to the graph domain. In the following, we summarize their approach. As before, n is the number of data points. We introduce the matrix $U = (\mathbf{u}_1, \dots, \mathbf{u}_n)^T \in \mathbb{R}^{n \times K}$. Here, the k th component of $\mathbf{u}_i \in \mathbb{R}^K$ is the strength for data point i to belong to class k . For each node i , the vector \mathbf{u}_i has to be an element of the Gibbs simplex Σ^K

$$\Sigma^K := \left\{ (x_1, \dots, x_K)^T \in [0, 1]^K \left| \sum_{k=1}^K x_k = 1 \right. \right\}.$$

The Ginzburg–Landau energy functional on graphs in (6) generalizes to the multiclass case as

$$E(U) = \frac{\varepsilon}{2} \langle U, L_s U \rangle + \frac{1}{\varepsilon} \psi(U) + F(\hat{U}, U). \quad (19)$$

Here,

$$\langle U, L_s U \rangle = \text{trace}(U^T L_s U)$$

measures variations in the vector field, the potential term

$$\psi(U) = \frac{1}{2} \sum_{i \in V} \left(\prod_{k=1}^K \frac{1}{4} \|\mathbf{u}_i - \mathbf{e}_k\|_{L_1}^2 \right)$$

drives the system closer to the pure phases, and the fidelity term

$$F(\hat{U}, U) = \sum_{i \in V} \frac{\omega}{2} \|\hat{\mathbf{u}}_i - \mathbf{u}_i\|_{L_2}^2$$

enables the encoding of a priori information with $\hat{U} = (\hat{\mathbf{u}}_1, \dots, \hat{\mathbf{u}}_n)^T$ representing the learned data. In the potential term, $\mathbf{e}_k \in \mathbb{R}^K$ is the vector whose k th component equals one and all other components vanish. The vectors $\mathbf{e}_1, \dots, \mathbf{e}_K$ correspond to the pure phases. Note that the authors use an L_1 -norm for the potential term as it prevents an undesirable minimum from occurring at the center of the simplex, as would be the case with an L_2 -norm for large K .

As in Section III, the authors use a convexity splitting scheme to minimize the Ginzburg–Landau functional in the phase-field approach. For this, the energy (19) is split as

$$E(U) = E_1(U) - E_2(U)$$

with

$$E_1(U) = \frac{\varepsilon}{2} \langle U, L_s U \rangle + \frac{c}{2} \langle U, U \rangle$$

and

$$E_2(U) = -\frac{1}{\varepsilon} \psi(U) - F(\hat{U}, U) + \frac{c}{2} \langle U, U \rangle.$$

In order to guarantee the convexity of the energy terms, we require $c \geq \omega + \frac{1}{\varepsilon}$. The convexity splitting scheme results in

$$\frac{U - \bar{U}}{\tau} + \varepsilon L_s U + cU = -\frac{1}{2\varepsilon} T(\bar{U}) + c\bar{U} + \omega(\hat{U} - \bar{U}), \quad (20)$$

where the elements T_{ik} of the matrix $T(\bar{U})$ are given as

$$T_{ik} = \sum_{l=1}^K \frac{1}{2} (1 - 2\delta_{kl}) \|\bar{\mathbf{u}}_i - \mathbf{e}_l\|_{L_1} \prod_{m=1, m \neq l}^K \frac{1}{4} \|\bar{\mathbf{u}}_i - \mathbf{e}_m\|_{L_1}^2.$$

Again, we assume that all values U are evaluated at the new time-point whereas \bar{U} indicates the previous time-point. Multiplying (20) by Φ^T from the left and using the eigendecomposition $L_s = \Phi \Lambda \Phi^T$, we obtain

$$U = B^{-1} \left[(1 + c\tau)\bar{U} - \frac{\tau}{2\varepsilon} \Phi^T T(\bar{U}) + \tau\omega(\hat{U} - \bar{U}) \right], \quad (21)$$

where all calligraphic fonts have the meaning $\mathcal{U} = \Phi^T U$. Since $B = (1 + c\tau)I + \varepsilon\tau\Lambda$ is a diagonal matrix with positive entries, its inverse is easy to apply.

After the update, we have to project the solution back to the Gibbs simplex Σ^K . In order to do this, we use of the projection procedure in [39]. For the initialization of the segmentation problem, we first assign random values from the standard uniform distribution on $(0, 1)$ to the nodes. Then, we project the result to the Gibbs simplex Σ^K and set the values in the fidelity points to the pure phases. Here, we finish the presentation of the model proposed in [4], [5]. Next, we extend this approach to the use of non-smooth potentials.

B. Vector-valued non-smooth diffuse interface methods

In this section, we extend the approach above to the use of non-smooth potentials. We start with the continuous setting. The potential function in (18) is now given as

$$\psi(\mathbf{u}) = \begin{cases} \psi_0(\mathbf{u}) & \mathbf{u} \in \Sigma^K, \\ \infty & \text{otherwise,} \end{cases} \quad (22)$$

where the smooth part is given as $\psi_0(\mathbf{u}) = -\frac{1}{2} \mathbf{u} \cdot T \mathbf{u}$. Here, $T \in \mathbb{R}^{K \times K}$ is a symmetric matrix, which contains constant interaction parameters T_{ij} . From physical considerations, T must have at least one positive eigenvalue. A typical choice is $T = I - \mathbf{1}\mathbf{1}^T$ with $\mathbf{1} = (1, \dots, 1)^T \in \mathbb{R}^K$ and the identity matrix $I \in \mathbb{R}^{K \times K}$, which means that the interaction between all different components is equal and no self-interaction occurs. In the numerical examples, we work with this choice

of T .

As before in the scalar case, we propose to regularize the energy with a Moreau–Yosida penalty term and obtain

$$E(\mathbf{u}_\nu) = \int \frac{\varepsilon}{2} \sum_{i=1}^K |\nabla u_{\nu,i}|^2 + \frac{1}{\varepsilon} \psi_0(\mathbf{u}_\nu) + \frac{1}{2\nu} \sum_{i=1}^K |\min(0, u_{\nu,i})|^2 dx. \quad (23)$$

Here, ν is again the penalty parameter. Applying the convexity splitting scheme to (23) in the same way as in the non-smooth scalar case, we obtain the following time-discrete scheme

$$\frac{u_{\nu,i} - \bar{u}_{\nu,i}}{\tau} - \varepsilon \Delta u_{\nu,i} + c u_{\nu,i} + \theta_\nu(u_{\nu,i}) = \frac{1}{\varepsilon} (T\bar{\mathbf{u}})_i + c \bar{u}_i + \omega(\hat{u}_i - \bar{u}_i) \quad (24)$$

for $i = 1, \dots, K$, where

$$\theta_\nu(u_{\nu,i}) := \frac{1}{\nu} \min(0, u_{\nu,i}).$$

In order to guarantee the convexity of the energy terms, we require $c \geq \omega$.

Next, if we write (24) in the form $F_i(u_{\nu,i}) = 0$ for $i = 1, \dots, K$, the semi-smooth Newton system

$$u_{\nu,i}^{(l+1)} = u_{\nu,i}^{(l)} - G_i(u_{\nu,i}^{(l)})^{-1} F_i(u_{\nu,i}^{(l)})$$

is given as

$$G_i(u_{\nu,i}^{(l)}) u_{\nu,i}^{(l+1)} = (c + \frac{1}{\tau}) \bar{u}_i + \frac{1}{\varepsilon} (T\bar{\mathbf{u}})_i + \omega(\hat{u}_i - \bar{u}_i),$$

where $G_i(u_{\nu,i}^{(l)}) := (c + \frac{1}{\tau})I - \varepsilon \Delta + \frac{1}{\nu} \chi_{\mathcal{A}(u_{\nu,i}^{(l)})}$ with

$$\mathcal{A}(u_{\nu,i}^{(l)}) := \{x \in \Omega : u_{\nu,i}^{(l)}(x) < 0\}.$$

This is the classical problem formulation. In the graph domain, (24) reads

$$\frac{\mathbf{u}_{\nu,i} - \bar{\mathbf{u}}_{\nu,i}}{\tau} + \varepsilon L_s \mathbf{u}_{\nu,i} + c \mathbf{u}_{\nu,i} + \theta_\nu(\mathbf{u}_{\nu,i}) = \frac{1}{\varepsilon} (T\bar{U}^T)_i + c \bar{\mathbf{u}}_i + \omega(\hat{\mathbf{u}}_i - \bar{\mathbf{u}}_i) \quad (25)$$

for $i = 1, \dots, K$, where $\bar{U} = (\bar{\mathbf{u}}_1, \dots, \bar{\mathbf{u}}_K) \in \mathbb{R}^{n,K}$ similar to the previous section and

$$(T\bar{U}^T)_i = - \sum_{j=1, j \neq i}^K \bar{\mathbf{u}}_j.$$

The resulting Newton system is given as

$$G_i(\mathbf{u}_{\nu,i}^{(l)}) \mathbf{u}_{\nu,i}^{(l+1)} = (c + \frac{1}{\tau}) \bar{\mathbf{u}}_i + \frac{1}{\varepsilon} (T\bar{U}^T)_i + \omega(\hat{\mathbf{u}}_i - \bar{\mathbf{u}}_i), \quad (26)$$

where $G_i(\mathbf{u}_{\nu,i}^{(l)}) := (c + \frac{1}{\tau})I + \varepsilon L_s + \frac{1}{\nu} \chi_{\mathcal{A}(\mathbf{u}_{\nu,i}^{(l)})}$. Multiplying (26) by Φ^T from the left and using the eigendecomposition $L_s = \Phi \Lambda \Phi^T$, we obtain

$$G_i(\mathbf{u}_{\nu,i}^{(l)}) \mathcal{U}_{\nu,i}^{(l+1)} = (c + \frac{1}{\tau}) \bar{\mathcal{U}}_i + \frac{1}{\varepsilon} \Phi^T (T\bar{U}^T)_i + \omega(\hat{\mathcal{U}}_i - \bar{\mathcal{U}}_i),$$

where $G_i(\mathbf{u}_{\nu,i}^{(l)}) := (c + \frac{1}{\tau})I + \varepsilon \Lambda + \frac{1}{\nu} \Phi^T \chi_{\mathcal{A}(\mathbf{u}_{\nu,i}^{(l)})} \Phi$ and all calligraphic fonts have the meaning $\mathcal{U} = \Phi^T \mathbf{u}$. Since this requires the solution of a small $m \times m$ linear system, we make use of MATLAB's backslash command.

Finally, after each time step, we project the solution back to the Gibbs simplex Σ^K using the procedure in [39].

Here, we finish the discussion about diffuse interface methods on graphs. Next, we introduce the diffuse interface approach when applied to hypergraph based segmentation.

V. HYPERGRAPHS AND LAPLACIANS

In this section we want to show at how to generalize the before mentioned methodology to the case of hypergraphs.

A hypergraph is considered as $G = (V, E)$ with $V = \cup \{x_i\}$ a family of objects and E a family of subsets e of V such that $\cup_{e \in E} = V$. We call V the vertices and E the hyperedge set of G . If a weight $w(e)$ is associated with each hyperedge then the hypergraph is called weighted. We can also define the degree $d(x_j)$ as $d(x_j) = \sum_{\{e \in E: x_j \in e\}} w(e)$. Also the edge in a hypergraph has a degree which is simply $\delta(e) = |e|$. The matrix $H \in \mathbb{R}^{|V| \times |E|}$ is the incidence matrix of the hypergraph where the rows correspond to the vertices and the columns to the hyperedges. In most applications, the entry $H_{i,j}$ is equal to one if the vertex x_i is contained in the set that defines the hyperedge j , otherwise the entries are set to zero. In all our applications the set of hyperedges refers to the different attributes that describe the problem. The matrices D_V and D_E are diagonal matrices containing the degrees of the vertices and hyperedges, respectively. And the diagonal matrix W_H is the weight matrix containing the weights of the hyperedges. One can then define the adjacency matrix $HW_H H^T - D_V$.

One might now wonder why the introduction of a hypergraph is a useful concept in the segmentation of data. Previous work explicitly using hypergraphs is given in [40], [41]. We here want to point out that in fact most real-world examples are initially represented via hypergraphs be it the image segmentation mentioned earlier where each vertex, i.e., pixel, has an associated vector of RGB values or the congress voting records used in [3] where for each congressman the voting record is stored in a feature vector. Since the incidence matrix of the hypergraph is naturally not square, in order to use the graph Laplacian the structure has to be transformed to a graph to represent pairwise relationships. To obtain pairwise relationships in both of these examples the computation of the square weight matrix W from (1) and hence the computation of the distance between two feature vectors for example allows a one-to-one relation between the different vertices and hence the segmentation via the graph Laplacian.

This means that in principal the methodology introduced earlier already takes hypergraph information that are then projected onto a simple graph where the information from the hyperedges is projected into the weight matrix W .

We here present an alternative approach to project the hypergraph information onto a graph, i.e., to create pairwise relationships of hypergraph data. This approach is based on

a relaxed problem that one considers instead of the NP hard cut problem. In more detail, one typically considers a relaxed optimization problem (cf. [40])

$$\operatorname{argmin}_{u \in \mathbb{R}^{|V|}} \frac{1}{2} \sum_{e \in E} \sum_{\{x_i, x_j\} \subseteq e} \frac{w(e)}{\delta(e)} \left(\frac{u(x_i)}{\sqrt{d(x_i)}} - \frac{u(x_j)}{\sqrt{d(x_j)}} \right)^2 \quad (27)$$

subject to

$$\sum_{x_j \in V} f(x_j)^2 = 1, \quad \sum_{x_j \in V} u(x_j) \sqrt{d(x_j)} = 0. \quad (28)$$

Defining the matrices $\Theta = D_V^{-1/2} H W_H D_E^{-1} H^T D_V^{-1/2}$ and $L_s = I - \Theta$ it was shown in [40] that

$$\sum_{e \in E} \sum_{\{x_i, x_j\} \subseteq e} \frac{w(e)}{\delta(e)} \left(\frac{u(x_i)}{\sqrt{d(x_i)}} - \frac{u(x_j)}{\sqrt{d(x_j)}} \right)^2 = u^T L_s u. \quad (29)$$

It is clear that due to W and D_E being diagonal matrices that the matrix L_s is symmetric and the definiteness follows from (29). If $u = 1$ in the set A and $u = -1$ in \bar{A} one obtains

$$u^T L_s u = \sum_{e \in E} \left(\sum_{\substack{x_i \in A, x_j \in \bar{A} \\ \text{or} \\ x_i \in \bar{A}, x_j \in A}} \frac{w(e)}{\delta(e)} \left(\frac{1}{\sqrt{d(x_i)}} + \frac{1}{\sqrt{d(x_j)}} \right) \right)^2 \quad (30)$$

$$+ \sum_{\substack{x_i \in A, \\ x_j \in A}} \frac{w(e)}{\delta(e)} \left(\frac{1}{\sqrt{d(x_i)}} - \frac{1}{\sqrt{d(x_j)}} \right)^2 \quad (31)$$

$$+ \sum_{\substack{x_i \in \bar{A}, \\ x_j \in \bar{A}}} \frac{w(e)}{\delta(e)} \left(\frac{-1}{\sqrt{d(x_i)}} + \frac{1}{\sqrt{d(x_j)}} \right)^2 \Bigg). \quad (32)$$

The last equation motivates the use of the diffuse interface approach as assuming that the degrees of the vertices are similar then (30) is the dominating term and hence minimization using the hypergraph Laplacian $u^T L_s u$ is achieved if the weights across the interface are minimal. We hence use the hypergraph Laplacian in the same way as the graph Laplacian for the segmentation of the vertices and run all diffuse interface models with the eigenvectors and eigenvalues of the hypergraph Laplacian instead of the graph Laplacian that could also be derived from hypergraph information. In the numerical experiments presented next we still use the original naming of the hypergraph and graph Laplacian even though both have been derived from hypergraph data.

VI. NUMERICAL EXPERIMENTS

The aim is to show that the methods introduced in this paper are effective and we chose to compare the smooth and non-smooth potential version of the diffuse interface method for graph-based and hypergraph-based problems. Bertozzi and Flenner compare the diffuse interface approach in [3] to many other techniques such as the p-Laplacian [42] with

favourable outcome for their approach. The computation of the eigenvalues is based on `eigs` from MATLAB, which uses the Lanczos process for $D^{-1/2} W D^{-1/2}$ in the graph case and for Θ in the hypergraph Laplacian. The results presented here are snapshots of a high-dimensional space of parameters that can be chosen and we want to illustrate the performance with respect to varying these parameters. Such parameters include the interface parameter ϵ , the number k of eigenvalues for the Laplacian, the convexity splitting parameter c , the (pseudo) time-step of the Allen–Cahn equation τ , as well as the correct stopping tolerance. One of the crucial questions is also the performance of the algorithms with respect to changes in the number of known or learned data.

A. Graphs

Graph-based segmentation has been used for both UCI datasets [43] and image based segmentation. We start with the scalar case for both a point set and an imaging problem. We later extend this to the multiclass segmentation.

Scalar segmentation: The first test we perform is based on the 65×65 image given in Figure 1(a). This image consists of two colors - here given by dark blue and yellow. The learned information of the image used as initial state for the smooth and non-smooth model is shown in Figure 1(b). The known image information is given by one pixel in the dark blue part and three pixels in the yellow part. Hence, the known image information constitutes only of 0.0947% of the whole image. The solution u of the smooth model is presented in Figure 1(c), while Figure 1(d) illustrates the final segmentation $\operatorname{sign}(u)$. The two corresponding results using the non-smooth model are given in Figure 1(e) and 1(f). The chosen parameters are given as $\omega_0 = 1$, $\varepsilon = 0.5$, $\tau = 0.01$, $\nu = 10^{-7}$, $c = 2\epsilon^{-1} + \omega_0$, $R = 21$, and $k = 5$. Here, R is the local scale for the graph Laplacian computation as used in (2). The computation of the eigenvalues is based on `svds` from MATLAB. As stopping criterion for the smooth and non-smooth model, we use

$$\frac{\|u - \bar{u}\|}{\|\bar{u}\|} \leq \epsilon_{tol}, \quad (33)$$

where we set $\epsilon_{tol} = 10^{-6}$, and we fix the maximum number of time steps to $t_{\max} = 500$. Note that for the non-smooth model, we fix a sequence of penalty parameters $\{\nu_q\}_{q \in \mathbb{N}}$ with $\nu_q \rightarrow 0$, and in each time step, we solve the problem $F(u_{\nu_q}) = 0$ for $q = 1, \dots, q_{\max}$ via a semi-smooth Newton method. In all examples, we use $\nu_1 = 10^{-1} \geq \nu_2 = 10^{-2} \geq \dots \geq \nu_{q_{\max}} = 10^{-7}$. Each semi-smooth Newton method is initialized by the approximate solution of the previous one. As stopping criterion for the semi-smooth Newton method, we use

$$\|F(u^{(l+1)})\| \leq \epsilon_{\text{rel}} \|F(u^{(0)})\| + \epsilon_{\text{abs}}, \quad l = 1, \dots, l_{\max}, \quad (34)$$

where we set $l_{\max} = 20$, $\epsilon_{\text{rel}} = 10^{-12}$, and $\epsilon_{\text{abs}} = 10^{-6}$. Finally, we solve the $k \times k$ systems of linear equations arising in each semi-smooth Newton step with MATLAB's backslash command.

The smooth model stops after $t_{\max} = 500$ time steps with $\frac{\|u - \bar{u}\|}{\|\bar{u}\|} = 9.5 \cdot 10^{-4}$. The CPU time is 2.6s and the minimum and maximum value of the solution are -1.165010

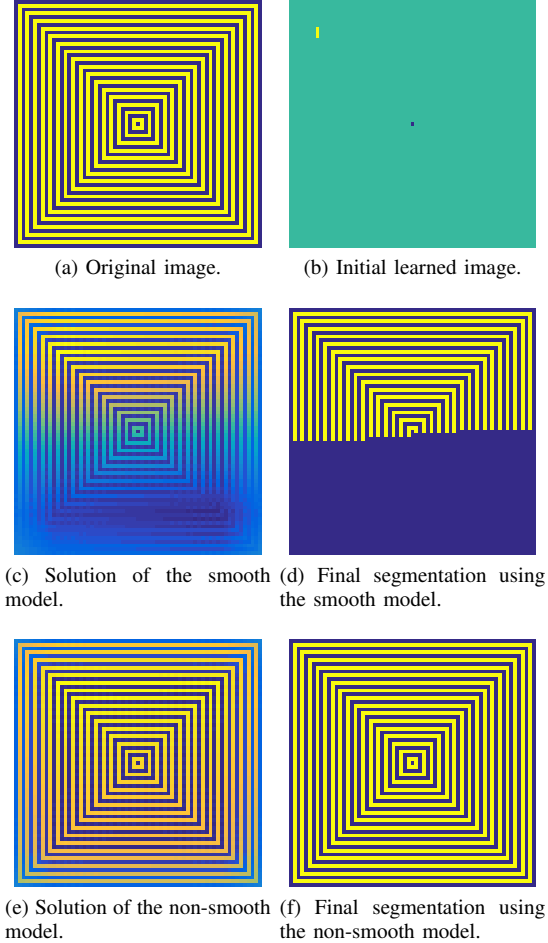


Fig. 1: Scalar image segmentation.

and 1.296961. The non-smooth model stops after $t_{\max} = 500$ time steps with $\frac{\|u - \bar{u}\|}{\|\bar{u}\|} = 8.6 \cdot 10^{-3}$. The CPU time is 173.2s and the minimum and maximum value of the solution are -1.000347 and 1.000116 . We observe that the concentrations stay closer within the interval $[-1, 1]$ when the non-smooth potential is used. Moreover, we clearly see from Figures 1(c)–1(f) that the segmentation using the smooth model is either unsuccessful or has not finished after 500 time steps. Before we will investigate this issue, we introduce the Figure of Certainty (FOC)

$$\text{FOC}(u_{\text{orig}}, p, q) = \frac{1}{n} \sum_{j=1}^n \frac{1}{1 + p \cdot |u_{\text{orig}}(j) - u_{\text{orig}}(s_i)|^q},$$

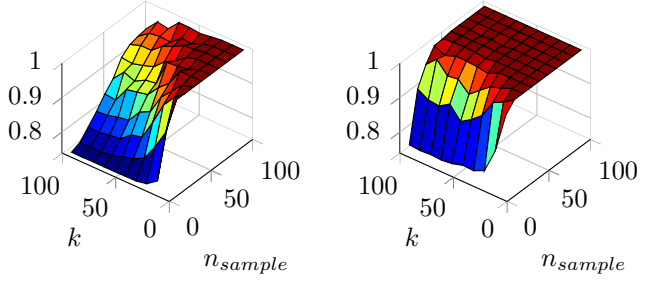
a quality measurement proposed by Strasters and Gerbrand [44] in order to evaluate the quality of segmentation. Here, u_{orig} is the original image, $p, q > 0$ are scaling parameters, $u_{\text{orig}}(j)$ represents the intensity of pixel j , and $u_{\text{orig}}(s_i)$ is the intensity representing the segment that comprises pixel j . It holds $\text{FOC} \in (0, 1]$, and the larger the FOC value is, the better is the segmentation. In the following, we use $p = q = 0.5$ if not mentioned otherwise. In the smooth case (Figure 1(d)), we obtain $\text{FOC} = 0.8186$ and in the non-smooth case (Figure 1(f)) $\text{FOC} = 1$. Now, we come back to the above mentioned issue that the smooth model is either unsuccessful or has not

finished after 500 time steps. We repeat the same simulation for the smooth model with $t_{\max} = 5000$ and $\epsilon_{\text{tol}} = 10^{-14}$. The simulation stops after 1776 time steps and a CPU time of 14.7s with $\frac{\|u - \bar{u}\|}{\|\bar{u}\|} = 9.9 \cdot 10^{-15}$ and $\text{FOC} = 0.8156$. Hence, the segmentation using the smooth model is unsuccessful with the used parameter set.

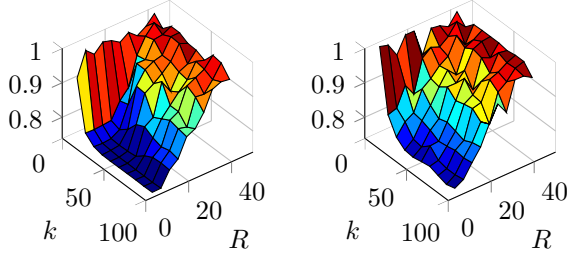
Next, we show the effect of varying different parameters. Each plot in Figure 2 shows the mean of the FOC values which were calculated for 10 runs with randomly chosen samples. In Figure 2(a) and 2(b), we vary the number of given sample points n_{sample} and the number of eigenvalues k for the smooth and non-smooth model. For both models, the segmentation performance increases as n_{sample} increases. We observe in the smooth case that if we reduce n_{sample} , then k should be reduced as well. This effect occurs in the non-smooth case only for the lower range of n_{sample} . The difference of both results is illustrated in Figure 3(a). Negative values indicate that the non-smooth potential performed better. Except for the case of small values of k and large values of n_{sample} , the non-smooth model outperforms the smooth one. In Figure 2(c) and 2(d), we vary the number of eigenvalues k and the distance R which was a local scale for the graph Laplacian computation, for the smooth and non-smooth model. For both models, the segmentation performance increases as R increases. Small values of k give better results with the non-smooth model. The difference of both results is illustrated in Figure 3(b). In almost every case, the non-smooth model outperforms the smooth one. In Figure 2(e) and 2(f), we vary the interface parameter ϵ and the fidelity parameter ω_0 for the smooth and non-smooth model. For both models, the segmentation performance increases as ϵ decreases. The difference of both results is illustrated in Figure 3(c). In most cases, the non-smooth model outperforms the smooth one.

Next, we consider a problem with a point set. If not mentioned otherwise, we use the same parameters and stopping criterion as in the previous example. The test is based on the point set given in Figure 4(a), which consists of 3000 data points in total. We have two kinds of points, the red ones and the blue ones, whereby each class contains 1500 points. The damaged data set used as initial state for the smooth and non-smooth model is shown in Figure 4(b). The known information is given by 10 data points for each class. Hence, the known data information constitutes only of 0.6667% of the whole data set. The final segmentation using the smooth and non-smooth model are presented in Figure 4(c) and 4(d), respectively. The chosen parameters are given as $\omega_0 = 1$, $\epsilon = 0.5$, $\tau = 0.01$, $\nu = 10^{-7}$, $c = 3\epsilon^{-1} + \omega_0$, $R = 9$, $k = 15$, and $t_{\max} = 400$. The smooth model was not able to correctly classify the area around $(-0.75, -0.6)$. This is exactly the area of a large gap in the initial data, as seen in Figure 4(b).

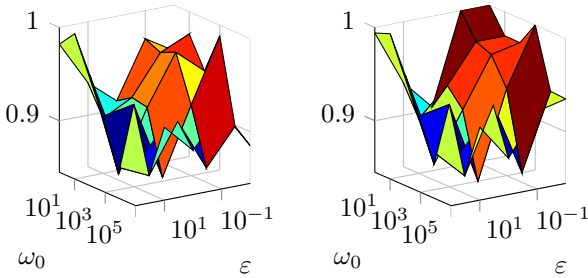
Next, we show the effect of varying different parameters. Each plot in Figure 5 shows the mean of the number of misclassified points which were calculated for 10 runs with randomly chosen samples. In Figure 5(a) and 5(b), we vary the number of given sample points n_{sample} and the number



(a) Mean FOC values using the smooth model. (b) Mean FOC values using the non-smooth model.



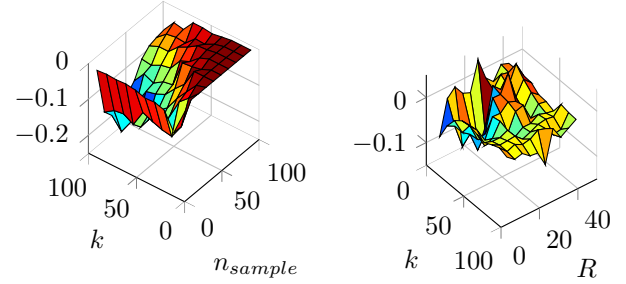
(c) Mean FOC values using the smooth model. (d) Mean FOC values using the non-smooth model.



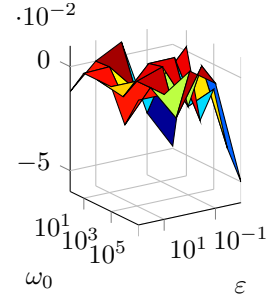
(e) Mean FOC values using the smooth model. (f) Mean FOC values using the non-smooth model.

Fig. 2: Comparison of the smooth and non-smooth model: The mean of the FOC values for the smooth (left column) and non-smooth (right column) model for varying parameters. For each (x, y) pair, we have taken 10 runs with randomly chosen samples.

of eigenvalues k for the smooth and non-smooth model. For both models, the segmentation performance increases as n_{sample} increases. For small values of n_{sample} , the non-smooth model performs better, whereas the smooth model gives better results for larger values of the pair (n_{sample}, k) . This can be seen in Figure 6(a), which shows the difference of both results. Negative values indicate that the non-smooth potential performed better. In Figure 5(c) and 5(d), we vary the number of eigenvalues k and the distance R for the smooth and non-smooth model. For both models, the segmentation performance is the best for $k = 10$. The difference of both results is illustrated in Figure 6(b). In almost every case, the non-smooth model outperforms the smooth one. In Figure 5(e) and 5(f), we vary the interface parameter ε and the fidelity parameter ω_0 for the smooth and non-smooth model. For both models, the segmentation performance increases as ε and ω_0 increase. The difference of both results is illustrated in Figure

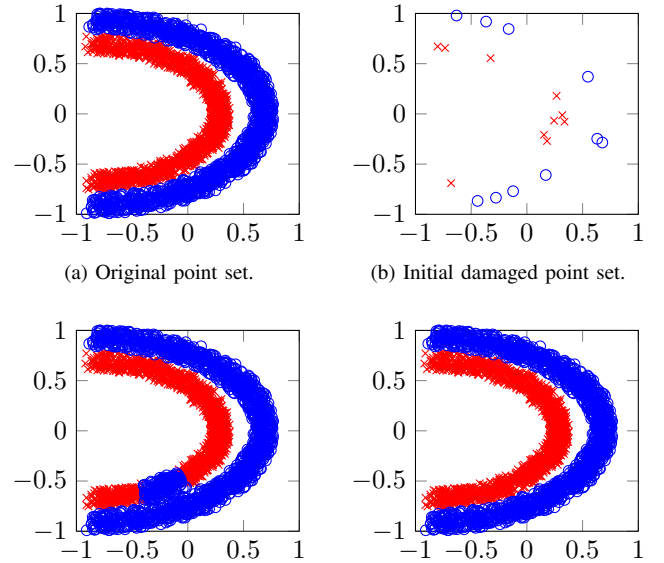


(a) Difference of the results in Figure 2(a) and 2(b). (b) Difference of the results in Figure 2(c) and 2(d).



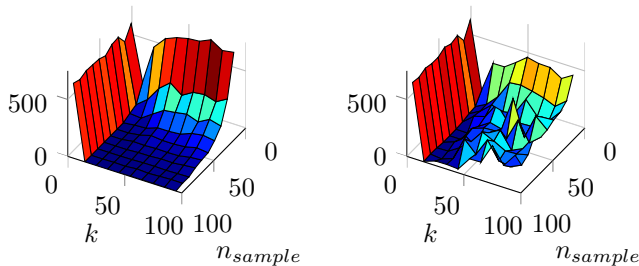
(c) Difference of the results in Figure 2(e) and 2(f).

Fig. 3: The differences between the mean for the smooth and non-smooth model with respect to the results in Figure 2. Negative values indicate that the non-smooth potential performed better.

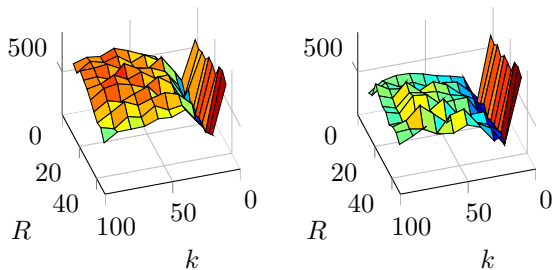


(c) Final segmentation using the smooth model. (d) Final segmentation using the non-smooth model.

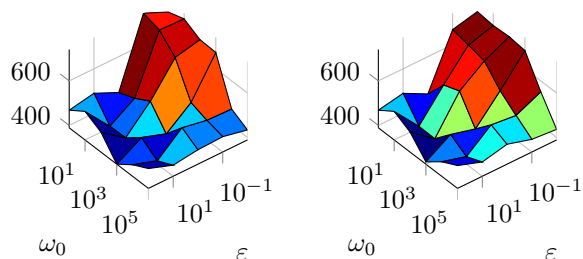
Fig. 4: Segmentation of a point set into two classes.



(a) Mean of the misclassification using the smooth model. (b) Mean of the misclassification using the non-smooth model.



(c) Mean of the misclassification using the smooth model. (d) Mean of the misclassification using the non-smooth model.



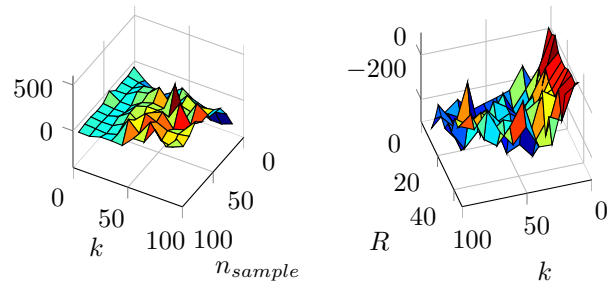
(e) Mean of the misclassification using the smooth model. (f) Mean of the misclassification using the non-smooth model.

Fig. 5: Comparison of the smooth and non-smooth model: The mean of the misclassification for the smooth (left column) and non-smooth (right column) model for varying parameters. For each (x, y) pair, we have taken 10 runs with randomly chosen samples.

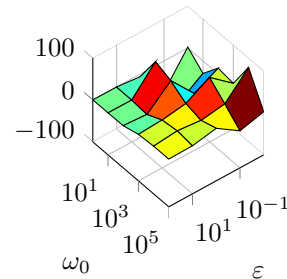
6(c). Both models behave similar.

Multiclass segmentation: We show in Figure 7 the results for a segmentation problem into four classes into the four corners.² We here vary the number of used eigenvalues of the graph Laplacian as well as the number of samples. We uniformly take the values $n_{sample} = 5, 10, \dots, 50$ and $k = 5, 10, \dots, 50$. It can be seen that with an increase in the number of both n_{sample} and k the misclassification is dramatically reduced. Here the one axis shows the variation in n_{sample} and the other the variation in k . For the mean we have taken 10 runs with randomly chosen samples. Figure 7 also shows the difference in the means between the non-smooth and the smooth potential. It can be seen that for sufficient information with larger sample and eigenvalues size the dif-

²The data are generated using the MATLAB code <http://de.mathworks.com/matlabcentral/fileexchange/41459-6-functions-for-generating-artificial-datasets>.



(a) Difference of the results in Figure 5(a) and 5(b). (b) Difference of the results in Figure 5(c) and 5(d).



(c) Difference of the results in Figure 5(e) and 5(f).

Fig. 6: The differences between the mean for the smooth and non-smooth model with respect to the results in Figure 5. Negative values indicate that the non-smooth potential performed better.

ference is neglectable but for smaller values of n_{sample} the non-smooth potential performs better for increasing values of k than the smooth potential. The chosen values are $\omega_0 = 10000$, $\nu = 10^{-7}$, $\epsilon = 10^1$, $\tau = 0.1$, and $c = (2/\epsilon) + \omega_0$.

B. Hypergraph Laplacian

We now want to present results for our approach regarding hypergraphs where both the case of a smooth and non-smooth potentials are tested.

Scalar segmentation: We here focus our attention on two datasets. The first dataset is the so-called `mushroom` dataset³ as introduced by Schlimmer [45], [43]. The dataset includes descriptions of hypothetical samples species of mushrooms. The goal is to identify each species as edible or non-edible. The latter includes definitely poisonous, unknown edibility, and not recommended. There is no simple or at least safe rule to determine which class a mushroom belongs to. The dataset we used contains 4062 mushroom species with 21 attributes, e.g. one attribute is the cap shape with the attribute values bell, conical, flat, knobbed and sunken. Similar to [40] we create a hyperedge whenever one or more species share the same value of a particular attribute. We simply set the entries in the corresponding column in H to 1. Based on this adjacency matrix and a weight vector with constant weight one we obtain the hypergraph Laplacian L_s . For the computation

³We obtain a MATLAB version of the data from <http://people.whitman.edu/~hundletr/courses/M350F14/M350/mushrooms.mat>.

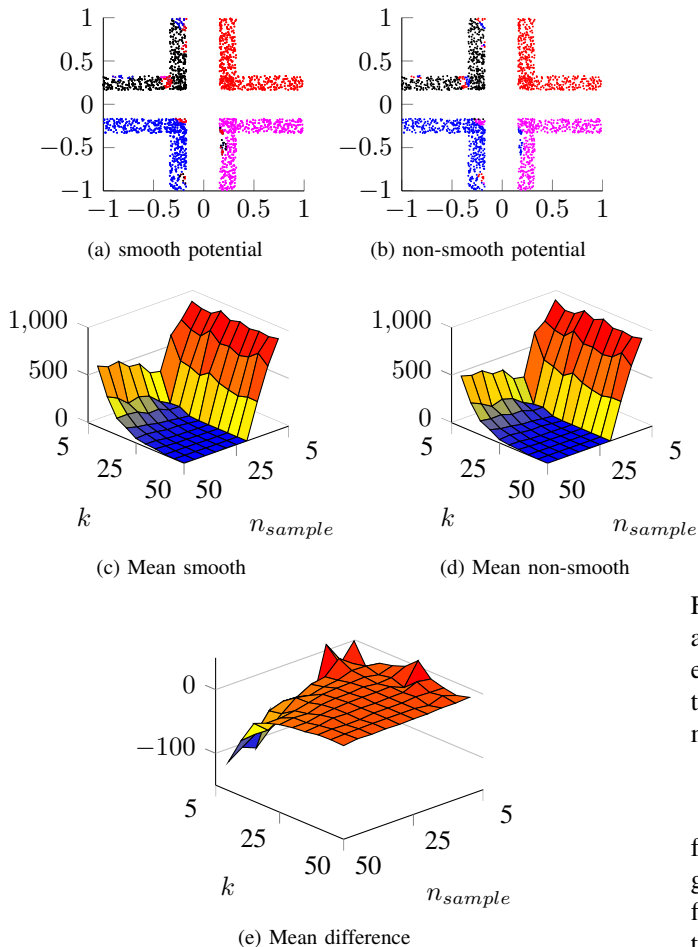


Fig. 7: Comparison of the smooth (a) and non-smooth (b) potential. In total 2000 points are segmented into 4 clusters with 15 given sample points for each cluster. With $R = 9$ and the number of used eigenvalues at 55 we obtained 109 misclassified points in the non-smooth case and 137 in the smooth case. The difference between the mean for non-smooth (d) and smooth (c) potential is shown in (e). Negative values indicate that the non-smooth potential performed better.

of the hypergraph Laplacian⁴ we use the Matlab functions based on [41]. The results shown in Figure 8 illustrate that our approach utilizing the hypergraph Laplacian allows for a solution to the segmentation problem. The performance both for the smooth and the non-smooth potential gets better with an increasing number of samples. The difference between both is almost neglectable even though the non-smooth potential gives slightly better results for small sample sizes but at a higher cost due to the nonlinear iteration at its core. The parameters for both methods are chosen as $\omega_0 = 10^5$, $\tau = 0.1$ $c = (3/\epsilon) + \omega_0$, and $\nu = 1e - 3$. The second example is also taken from the UCI machine learning repository [43] and is the so-called student performance data set as introduced in [46]. The data is given for 395 students with attributes ranging from

⁴The MATLAB code is given under <http://www.ml.uni-saarland.de/code/hypergraph/hypergraphcut.zip>.

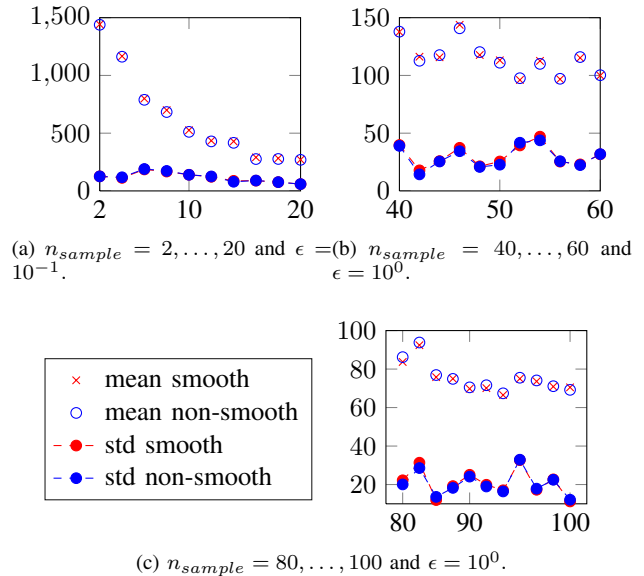
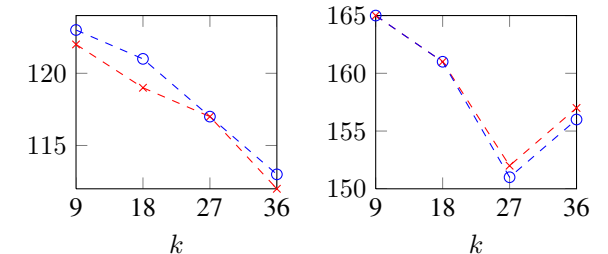
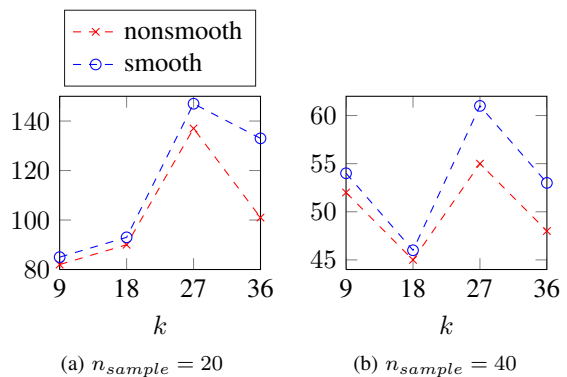


Fig. 8: Comparison of the misclassification of the smooth (a) and non-smooth (b) potential for the mushroom hypergraph example. We vary the number of sample points and see that for both schemes the results behave similar and the misclassification reduces.

family size to the job of the parents. All in all 30 attributes are given with three additional columns noting the grades for the first period, the second period, and the final grade. We follow the approach given in [46] by adding these information to the basis on which the hypergraph is formed. Again for all 30 attributes one or more pupils share a hyperedge whenever they share an attribute value. Additionally, we include hyperedges for the pupils with the same grades based on the first and/or second period. We always run 5 tests for each scenario and show the mean in Figure 9. The parameters for this example are given via $\omega_0 = 10^8$, $\epsilon = 10^{-2}$, $\tau = 0.1$, $c = (3/\epsilon) + \omega_0$ and $\nu = 10^{-6}$. We also show the difference in the eigenvalues of the hypergraph Laplacian and the graph Laplacian using a weight matrix W . In order to generate the matrix W we take the feature vector for each of the 395 pupils and use (1). In Figure 10 we show the difference in the smallest non-zero eigenvalues of the two Laplacians as well as the separation for the school example when the graph Laplacian is used. The parameters are set to $\omega_0 = 10^8$, $\epsilon = 10^{-2}$, $\tau = 0.1$, $c = (3/\epsilon) + \omega_0$ and $\nu = 10^{-6}$. It can be seen that the segmentation improves with an increasing number of eigenvectors and we note that we have chosen the same parameters as for the hypergraph Laplacian. It is not clear whether this parameter constellation is the best possible as in this setup the hypergraph Laplacian outperforms the graph Laplacian.

Multiclass segmentation: We again use an example from the UCI ML repository. In particular, we focus on the zoo dataset introduced in [47]. This dataset contains 101 individuals with 18 attributes such number of legs or whether they have hair. The segmentation is performed into 7 classes that are already



(c) $n_{sample} = 40$ without attribute 32. (d) $n_{sample} = 40$ without attribute 31 and 32.

Fig. 9: Comparison of the misclassification of the smooth (a) and non-smooth (b) potential for the student performance hypergraph example. We vary the number of sample points and see that for both schemes the results behave similar and the misclassification reduces.

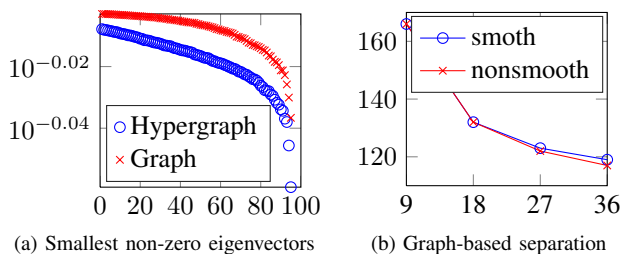


Fig. 10: Comparison of the eigenvalues of the hypergraph Laplacian and the graph Laplacian applied to the school example. The right picture shows the misclassification for the graph Laplacian based segmentation using an increased number of eigenvalues and a sample size $n_{sample} = 40$.

pre-specified. We want our algorithm to segment the data into these 7 classes given only a small number of samples from each class. Figure 11 shows the results for a small number of samples for each class as well as a varying number of eigenvectors of the hypergraph Laplacian. We also test two different values of the interface parameter ϵ . The results for the non-smooth potential tend to be slightly better than for the smooth potential, especially when the number of eigenvectors grows. We have set the parameters to $\omega_0 = 100$, $\epsilon = 10^{-1}$, $\tau = 0.01$, $c = (3/\epsilon) + \omega_0$, and $\nu = 10^{-4}$ in this example.

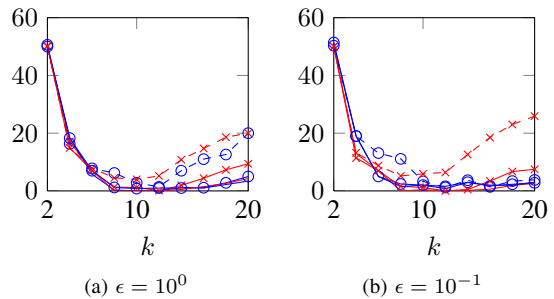


Fig. 11: Comparison of the misclassification of the mean of 10 runs of the smooth vs. non-smooth potential. Blue lines represent the non-smooth and the red ones the smooth potentials. Dashed lines correspond to one given sample point, solid lines with markers to two given sample points, and solid lines alone to three given sample points per class. Shown is the total misclassification against the number of eigenvectors used. The left plot is for $\epsilon = 10^0$ and the right one for $\epsilon = 10^{-1}$.

CONCLUSIONS AND OUTLOOK

We have shown that diffuse interface methods while already being very powerful can be further generalized. We illustrated that non-smooth potentials are a viable option for the separation of data. While the computations become more expensive due to the nonlinearity that is treated with the semi-smooth Newton scheme, the results in many cases show that the results are even better than for the smooth potential. Additionally, we showed that the methods are not limited to the graph Laplacian setup but can successfully be employed for the hypergraph Laplacian. Future work should incorporate more sophisticated eigenvalue methods and our goal is to further investigate different techniques for the segmentation of hypergraphs.

ACKNOWLEDGMENT

The third author would like to thank Cristina Garcia-Cardona for answering questions regarding her work on diffuse interface methods on graphs.

REFERENCES

- [1] D. Zhou and B. Schölkopf, "A regularization framework for learning from graph data," in *ICML Workshop on Statistical Relational Learning*, 2004, pp. 132–137.
- [2] D. I. Shuman, S. K. Narang, P. Frossard, A. Ortega, and P. Vandergheynst, "The emerging field of signal processing on graphs: Extending high-dimensional data analysis to networks and other irregular domains," *IEEE Signal Processing Mag.*, vol. 30, no. 3, pp. 83–98, 2013. [Online]. Available: <http://dx.doi.org/10.1109/MSP.2012.2235192>
- [3] A. L. Bertozzi and A. Flenner, "Diffuse interface models on graphs for classification of high dimensional data," *Multiscale Model. Simul.*, vol. 10, no. 3, pp. 1090–1118, 2012. [Online]. Available: <http://dx.doi.org/10.1137/11083109X>
- [4] C. Garcia-Cardona, E. Merkurjev, A. L. Bertozzi, A. Flenner, and A. G. Percus, "Multiclass data segmentation using diffuse interface methods on graphs," *IEEE Trans. Pattern Anal. Mach. Intell.*, vol. 36, no. 8, pp. 1600–1613, 2014. [Online]. Available: <http://dx.doi.org/10.1109/TPAMI.2014.2300478>
- [5] E. Merkurjev, C. Garcia-Cardona, A. L. Bertozzi, A. Flenner, and A. G. Percus, "Diffuse interface methods for multiclass segmentation of high-dimensional data," *Appl. Math. Lett.*, vol. 33, pp. 29–34, 2014. [Online]. Available: <http://dx.doi.org/10.1016/j.aml.2014.02.008>

- [6] J. E. Taylor and J. W. Cahn, "Linking anisotropic sharp and diffuse surface motion laws via gradient flows," *J. Statist. Phys.*, vol. 77, no. 1-2, pp. 183–197, 1994. [Online]. Available: <http://dx.doi.org/10.1007/BF02186838>
- [7] S. M. Allen and J. W. Cahn, "A microscopic theory for antiphase boundary motion and its application to antiphase domain coarsening," *Acta Metall.*, vol. 27, no. 6, pp. 1085–1095, 1979. [Online]. Available: [http://dx.doi.org/10.1016/0001-6160\(79\)90196-2](http://dx.doi.org/10.1016/0001-6160(79)90196-2)
- [8] A. L. Bertozzi, S. Esedoğlu, and A. Gillette, "Inpainting of binary images using the cahn–hilliard equation," *IEEE Trans. Image Process.*, vol. 16, no. 1, pp. 285–291, 2007. [Online]. Available: <http://dx.doi.org/10.1109/TIP.2006.887728>
- [9] S. Esedoğlu and Y.-H. R. Tsai, "Threshold dynamics for the piecewise constant Mumford–Shah functional," *J. Comput. Phys.*, vol. 211, no. 1, pp. 367–384, 2006. [Online]. Available: <http://dx.doi.org/10.1016/j.jcp.2005.05.027>
- [10] T. F. Chan and L. A. Vese, "Active contours without edges," *IEEE Trans. Image Process.*, vol. 10, no. 2, pp. 266–277, 2001. [Online]. Available: <http://dx.doi.org/10.1109/83.902291>
- [11] T. F. Chan and J. Shen, "Nontexture inpainting by curvature-driven diffusions," *J. Vis. Commun. Image Represent.*, vol. 12, no. 4, pp. 436–449, 2001. [Online]. Available: <http://www.sciencedirect.com/science/article/pii/S1047320301904870>
- [12] M. Hein and T. Bühler, "An inverse power method for nonlinear eigenproblems with applications in 1-spectral clustering and sparse PCA," in *Advances in Neural Information Processing Systems*, 2010, pp. 847–855.
- [13] C. M. Elliott and H. Garcke, "On the Cahn–Hilliard equation with degenerate mobility," *SIAM J. Math. Anal.*, vol. 27, no. 2, pp. 404–423, 1996. [Online]. Available: <http://dx.doi.org/10.1137/S0036141094267662>
- [14] L. Blank, M. Butz, H. Garcke, L. Sarbu, and V. Styles, "Allen–Cahn and Cahn–Hilliard variational inequalities solved with optimization techniques," in *Constrained Optimization and Optimal Control for Partial Differential Equations*. Springer, 2012, pp. 21–35. [Online]. Available: http://dx.doi.org/10.1007/978-3-0348-0133-1_2
- [15] J. Bosch, D. Kay, M. Stoll, and A. J. Wathen, "Fast solvers for Cahn–Hilliard inpainting," *SIAM J. Imaging Sci.*, vol. 7, no. 1, pp. 67–97, 2014. [Online]. Available: <http://dx.doi.org/10.1137/130921842>
- [16] J. Bosch and M. Stoll, "A fractional inpainting model based on the vector-valued Cahn–Hilliard equation," *SIAM J. Imaging Sci.*, no. 4, pp. 2352–2382, 2015. [Online]. Available: <http://dx.doi.org/10.1137/15M101405X>
- [17] M. Hintermüller, K. Ito, and K. Kunisch, "The primal-dual active set strategy as a semismooth Newton method," *SIAM J. Optim.*, vol. 13, no. 3, pp. 865–888, 2002. [Online]. Available: <http://dx.doi.org/10.1137/S1052623401383558>
- [18] F. R. K. Chung, *Spectral graph theory*, ser. CBMS Regional Conference Series in Mathematics. Providence, RI: Amer. Math. Soc., 1997, vol. 92.
- [19] U. von Luxburg, "A tutorial on spectral clustering," *Stat. Comput.*, vol. 17, no. 4, pp. 395–416, 2007. [Online]. Available: <http://dx.doi.org/10.1007/s11222-007-9033-z>
- [20] G. H. Golub and C. F. Van Loan, *Matrix computations*, 3rd ed., ser. Johns Hopkins Studies in the Mathematical Sciences. Baltimore, MD: Johns Hopkins Univ. Press, 1996.
- [21] R. Lehoucq, D. Sorensen, and C. Yang, *ARPACK Users' Guide*. SIAM, 1998. [Online]. Available: <http://epubs.siam.org/doi/abs/10.1137/1.9780898719628>
- [22] C. R. Anderson, "A Rayleigh–Chebyshev procedure for finding the smallest eigenvalues and associated eigenvectors of large sparse Hermitian matrices," *J. Comput. Phys.*, vol. 229, no. 19, pp. 7477–7487, 2010. [Online]. Available: <http://dx.doi.org/10.1016/j.jcp.2010.06.030>
- [23] P. Bochev and R. B. Lehoucq, "On the finite element solution of the pure Neumann problem," *SIAM Review*, vol. 47, no. 1, pp. 50–66, 2005. [Online]. Available: <http://dx.doi.org/10.1137/S0036144503426074>
- [24] M. A. Freitag and A. Spence, "A tuned preconditioner for inexact inverse iteration applied to Hermitian eigenvalue problems," *IMA J. Numer. Anal.*, vol. 28, no. 3, pp. 522–551, 2008. [Online]. Available: <http://imajna.oxfordjournals.org/content/28/3/522>
- [25] E. Merkurjev, T. Kostić, and A. L. Bertozzi, "An MBO scheme on graphs for classification and image processing," *SIAM J. Imaging Sci.*, vol. 6, no. 4, pp. 1903–1930, 2013. [Online]. Available: <http://dx.doi.org/10.1137/120886935>
- [26] C. Fowlkes, S. Belongie, F. Chung, and J. Malik, "Spectral grouping using the Nyström method," *IEEE Trans. Pattern Anal. Mach. Intell.*, vol. 26, no. 2, pp. 214–225, 2004. [Online]. Available: <http://dx.doi.org/10.1109/TPAMI.2004.1262185>
- [27] C. Fowlkes, S. Belongie, and J. Malik, "Efficient spatiotemporal grouping using the Nyström method," in *Proc. 2001 IEEE Conf. Computer Vision and Pattern Recognition*, vol. 1. IEEE, 2001, pp. 1–231. [Online]. Available: <http://dx.doi.org/10.1109/CVPR.2001.990481>
- [28] L. Zelnik-Manor and P. Perona, "Self-tuning spectral clustering," in *Advances in Neural Information Processing Systems 17*. Cambridge, MA: MIT Press, 2004, pp. 1601–1608.
- [29] J. W. Cahn and J. E. Hilliard, "Free energy of a nonuniform system. I. Interfacial free energy," *J. Chem. Phys.*, vol. 28, no. 2, pp. 258–267, 1958. [Online]. Available: <http://dx.doi.org/10.1063/1.1744102>
- [30] X. Wang and Q. Du, "Modelling and simulations of multi-component lipid membranes and open membranes via diffuse interface approaches," *J. Math. Biol.*, vol. 56, no. 3, pp. 347–371, 2008. [Online]. Available: <http://dx.doi.org/10.1007/s00285-007-0118-2>
- [31] J. A. Dobrosotskaya and A. L. Bertozzi, "A wavelet-Laplace variational technique for image deconvolution and inpainting," *IEEE Trans. Image Process.*, vol. 17, no. 5, pp. 657–663, 2008. [Online]. Available: <http://dx.doi.org/10.1109/TIP.2008.919367>
- [32] Y. Li, D. Jeong, J.-i. Choi, S. Lee, and J. Kim, "Fast local image inpainting based on the Allen–Cahn model," *Digit. Signal Process.*, vol. 37, pp. 65–74, 2015. [Online]. Available: <http://dx.doi.org/10.1016/j.dsp.2014.11.006>
- [33] Y. van Gennip, N. Guillen, B. Osting, and A. L. Bertozzi, "Mean curvature, threshold dynamics, and phase field theory on finite graphs," *Milan J. Math.*, vol. 82, no. 1, pp. 3–65, 2014. [Online]. Available: <http://dx.doi.org/10.1007/s00032-014-0216-8>
- [34] X. Luo and A. L. Bertozzi, "Convergence analysis of the graph Allen–Cahn scheme," Dept. Math., Univ. of California Los Angeles, Los Angeles, CA, Tech. Rep., 2016.
- [35] C.-B. Schönlieb and A. L. Bertozzi, "Unconditionally stable schemes for higher order inpainting," *Commun. Math. Sci.*, vol. 9, no. 2, pp. 413–457, 2011. [Online]. Available: <http://dx.doi.org/10.4310/CMS.2011.v9.n2.a4>
- [36] D. J. Eyre, "Unconditionally gradient stable time marching the Cahn–Hilliard equation," in *MRS Proceedings*, vol. 529. Cambridge Univ Press, 1998, p. 39. [Online]. Available: <http://dx.doi.org/10.1557/PROC-529-39>
- [37] M. Hintermüller, M. Hinze, and M. H. Tber, "An adaptive finite-element Moreau–Yosida-based solver for a non-smooth Cahn–Hilliard problem," *Optim. Methods Softw.*, vol. 26, no. 4-5, pp. 777–811, 2011. [Online]. Available: <http://dx.doi.org/10.1080/10556788.2010.549230>
- [38] M. R. Hestenes and E. Stiefel, "Methods of conjugate gradients for solving linear systems," *J. Res. Nat. Bur. Stand.*, vol. 49, pp. 409–436, 1952.
- [39] Y. Chen and X. Ye, "Projection onto a simplex," *ArXiv e-prints:1101.6081*, 2011.
- [40] D. Zhou, J. Huang, and B. Schölkopf, "Learning with hypergraphs: Clustering, classification, and embedding," in *Advances in Neural Information Processing Systems 19*, 2006, pp. 1601–1608.
- [41] M. Hein, S. Setzer, L. Jost, and S. S. Rangapuram, "The total variation on hypergraphs - learning on hypergraphs revisited," in *Advances in Neural Information Processing Systems*, 2013, pp. 2427–2435.
- [42] A. Szlam and X. Bresson, "A total variation-based graph clustering algorithm for cheeger ratio cuts," Dept. Math., Univ. of California Los Angeles, Los Angeles, CA, Tech. Rep., 2009.
- [43] M. Lichman, "UCI machine learning repository," Irvine, CA, 2013. [Online]. Available: <http://archive.ics.uci.edu/ml>
- [44] K. C. Strasters and J. J. Gerbrands, "Three-dimensional image segmentation using a split, merge and group approach," *Pattern Recogn. Lett.*, vol. 12, no. 5, pp. 307–325, 1991. [Online]. Available: [http://dx.doi.org/10.1016/0167-8655\(91\)90414-H](http://dx.doi.org/10.1016/0167-8655(91)90414-H)
- [45] J. C. Schlimmer, "Concept acquisition through representational adjustment," Ph.D. dissertation, Dept. Comput. Inform. Sci., Univ. of California, Irvine, CA, 1987.
- [46] P. Cortez and A. M. G. Silva, "Using data mining to predict secondary school student performance," in *Proc. 5th Future Bus. Technol. Conf. Porto, Portugal: EUROSIS*, 2008, pp. 5–12. [Online]. Available: <http://hdl.handle.net/1822/8024>
- [47] R. S. Forsyth, "PC/BEAGLE User's Guide," *BUPA Med. Res. Ltd.*, 1990.